Surface self-diffusion induced sintering of nanoparticles

Xiaobo Chen,[1] Can Li,[2] Boyang Li,[3] Yubin Ying,[4] Shuonan Ye,[1] Dmitri N. Zakharov,[5] Sooyeon Hwang,[5] Jiye Fang,[2] Guofeng Wang,[3] Yong-Jie Hu,[4] Guangwen Zhou[1*]

[1]Materials Science and Engineering Program & Department of Mechanical Engineering, State University of New York at Binghamton, Binghamton, New York 13902, United States

[2]Department of Chemistry, State University of New York at Binghamton, Binghamton, New York 13902, United States

[3]Department of Mechanical Engineering and Materials Science, University of Pittsburgh, Pittsburgh, Pennsylvania 15261, United States

[4]Department of Material Science and Engineering, Drexel University, Philadelphia, Pennsylvania 19104, United States

[5]Center for Functional Nanomaterials, Brookhaven National Laboratory, Upton, New York 11973, United States

Abstract

Despite the critical role of sintering phenomena in constraining the long-term durability of nano-sized particles, a clear understanding of nanoparticle sintering has remained elusive due to the challenges in atomically tracking the neck initiation and discerning different mechanisms. Through the integration of in-situ transmission electron microscopy and atomistic modeling, this study uncovers the atomic dynamics governing the neck initiation of Pt-Fe nanoparticles via a surface self-diffusion process, allowing for coalescence without significant particle movement. Real-time imaging reveals that thermally activated surface morphology changes in individual nanoparticles induce significant surface self-diffusion. The kinetic entrapment of self-diffusing atoms in the gaps between closely spaced nanoparticles leads to the nucleation and growth of atomic layers for neck formation. This surface self-diffusion-driven sintering process is activated at a relatively lower temperature compared to the classic Ostwald ripening and particle migration and coalescence processes. The fundamental insights have practical implications for manipulating the morphology, size distribution, and stability of nanostructures by leveraging surface self-diffusion processes.

Keywords: Surface self-diffusion, Neck initiation, Sintering, Pt-Fe nanoparticles, In-situ TEM

* Correspondence to: gzhou@binghamton.edu

Introduction

The size effect of nanomaterials is widely acknowledged across various technological applications, including nanoscale electrics, optics, mechanics, and catalysts.[1–3] Nano-sized materials, characterized by a multitude of low-coordination sites, exhibit significant alternation in their physical and chemical properties compared to their bulk counterparts. However, the excessive surface free energy associated with these low coordinated sites destabilizes dispersed nanoparticles (NPs), leading to a pronounced inclination toward particle sintering.[4–8] Despite the availability of diverse experimental approaches for synthesizing size- and morphology-controlled NPs,[1,2] the intrinsic tendency for sintering remains a substantial hurdle, particularly concerning the long-term stability of NPs. Practical operation conditions, such as electrical, chemical, and thermal stimuli, can significantly expedite property degradation due to NP sintering.[5,6,9–12] To advance the designs and utilization of NPs, a fundamental understanding of the microscopic mechanisms governing the sintering behaviors of NPs is imperative.

The classic models of NP sintering have been largely based on post-mortem characterizations involving ensemble averages, lacking real-time atomic observations of the dynamic behaviors. The advancement of transmission electron microscopy (TEM) in recent years has enabled temperature- and time-resolved imaging of the sintering processes at the atomic-scale.[9,13–16] In-situ TEM observations have provided fundamental insights into the sintering dynamics of various NPs, including Pt,[17] Bi,[12]Au,[18–20] PdSi,[11] PbSe,[10] Au/TiO_2,[21,22] Pt/Al_2O_3,[23,24] Pt/C,[25] Cu/SiO_2,[26] among others. Such in-situ observations along with theoretical modeling have provided valuable insights into the mechanisms of sintering dynamics, including neck formation and coalescence promoted by surface diffusion.[27] However, the atomic-level and microscopic mechanisms underlying the neck initiation remains poorly understood. This knowledge gap stems from the lack of atomic details regarding mass transport leading to the initiation of neck formation, despite its critical importance for a comprehensive understanding of sintering kinetics.[7,18,28] The classical description of particle sintering primarily revolves around two proposed mechanisms: Ostwald ripening (OR) and particle migration and coalescence (PMC).[4,7] OR entails evaporation of atoms from small particles, subsequently captured by large particles, thereby leading to the growth of the big particles at the expense

of smaller ones. In contrast, PMC involves the Brownian-like motion of particles, with subsequent collisions leading to particle growth.

The majority of reported studies on sintering have focused on NPs with sizes < 10 nm and irregular morphologies. For such small sizes, the sintering through OR or PMC can be readily activated thermally. However, for larger particles (>10 nm), NP migration becomes more sluggish due to the substantial interfacial area between the NPs and the support.[7] Additionally, the melting temperatures of NPs increase significantly with size,[29] reducing the role of atomic evaporation for larger nanoparticles. Moreover, the driving force behind the ripening and sintering of NPs is to minimize the overall surface energy within an ensemble of NPs.[17,30–32] However, this global energy minimization treatment does not fully consider the evolving free energy landscape of individual NPs and its influence on specific sintering pathways.

In this work, we investigate how the inherent tendency of individual NPs to minimize their surface energy influences their morphological evolution and drives significant surface self-diffusion. This is particularly relevant to the initiation of necking between NPs that are already in close proximity. We focus on the sintering of NPs with relatively large sizes (> 10 nm) and well-developed crystal facets, at temperatures prior to the activation of OR or PMC processes. We present an NP sintering process induced by surface self-diffusion, resulting in neck initiation at inter-particle gaps. This process occurs in the absence of adatom diffusion from smaller to larger particles and direct particle collisions. The surface self-diffusion process reported here does not involve mass transfer between NPs, and thus, no diffusion occurs on the surface of the support. Additionally, it is more readily activated thermally compared to the OR process, which necessitates complete detachment/evaporation of atoms from NPs, and the PMC process, which requires particle migration. The sintering controlled by this surface self-diffusion process encompasses four key stages: i) proximity of NPs – This first step involves bringing NPs into close proximity, achieved either through high loading of NPs on a support or through thermally driven random migration of NPs under practically relevant thermal annealing conditions; ii) narrowing of the inter-particle gap – surface self-diffusion induces surface morphology evolution, leading to the entrapment of self-diffusing atoms in inter-particle gap regions; iii) neck initiation – this stage is characterized by the

84 nucleation and growth of atomic layers in the inter-particle gaps, initiating the formation of a neck; iv) neck
85 growth – this process is facilitated by surface and volume diffusion to lower the total system energy.
86 Atomic-scale observations and molecular dynamics (MD) simulations reveal that annealing temperature
87 and inter-particle spacing play a key role in controlling the NP sintering dynamics.

Results

Pt-Fe cubic NPs, synthesized through wet chemistry methods, serve as a model system due to their well-controlled shape and size and their potential applications that demand magnetic and catalytic properties.[33–36] The well-defined facets and superior crystallinity of the NPs offer significant advantages for assessing the sintering behaviors of NPs. Fig. 1a illustrates a low-magnification high-angle annular dark-field (HAADF)-scanning TEM (STEM) image of the as-loaded nano-cube $Pt_{85}Fe_{15}$ NPs. These NPs are drop-cast on an amorphous Si_3N_4 membrane, exhibiting relatively uniform size and morphology, with some well dispersed and others in closer proximity to each other (more examples in Fig. S1). Fig. 1b displays a representative atomic-scale HAADF image, showing the uniform image contrast of atomic columns. The observation confirms the single-phase, random distribution of Pt and Fe atoms in the NP. Fig.1c presents a high-resolution TEM (HRTEM) image of a typical $Pt_{85}Fe_{15}$ NP, wherein the uniform image contrast of the crystal lattice further verifies the random solid solution nature of the alloy. The measured interplanar spacing in Figs. 1b and 1c matches well with alloyed $Pt_{85}Fe_{15}$(200) lattice planes. The as-prepared $Pt_{85}Fe_{15}$ NPs are predominantly square or rectangular in shape, with a small fraction exhibiting irregular morphologies such as triangular or spherical forms. As depicted in the inset of Fig. 1c, nano-cube NPs account for ~ 80% of the total NPs (N = 264) examined by TEM. A minor fraction of NPs displays extended structure defects in the bulk, as exemplified by the five-fold twin boundaries in the HRTEM image of Fig. 1d (additional examples in Fig. S2). Both the HAADF and HRTEM images (Fig. 1 and S2) indicate that the surfaces of the as-synthesized NPs are not atomically flat. Instead, they exhibit a high density of atomic defects, such as atomic steps, kinks and adatoms, leading to variations in surface morphology at the atomic scale. Importantly, it is worth noting that these surface defects serve as the source for surface self-diffusion at elevated temperatures.

The size distribution of the as-loaded Pt-Fe NPs conforms to a Gaussian distribution with an arithmetic mean value of ~11.6 nm and a full-width at half-maximum of 2.4 nm, as illustrated in Fig. 1e. The average particle size is consistent with the estimate derived from the Debye-Scherer equation based on the full-width at half-maximum of synchrotron X-ray diffraction (XRD) patterns, as depicted in Fig. 1f.

The XRD measurements also reveal smaller d-spacings of the Pt-Fe NPs compared to those for pure Pt (PDF #04-0802). This is well consistent with Vegard's law[37,38] for the atomic composition of $Pt_{85}Fe_{15}$ NPs (composition measurements provided in Fig. S3). The absence of any superlattice lines in the XRD pattern confirms the random solid-solution nature of the $Pt_{85}Fe_{15}$ alloy NPs.

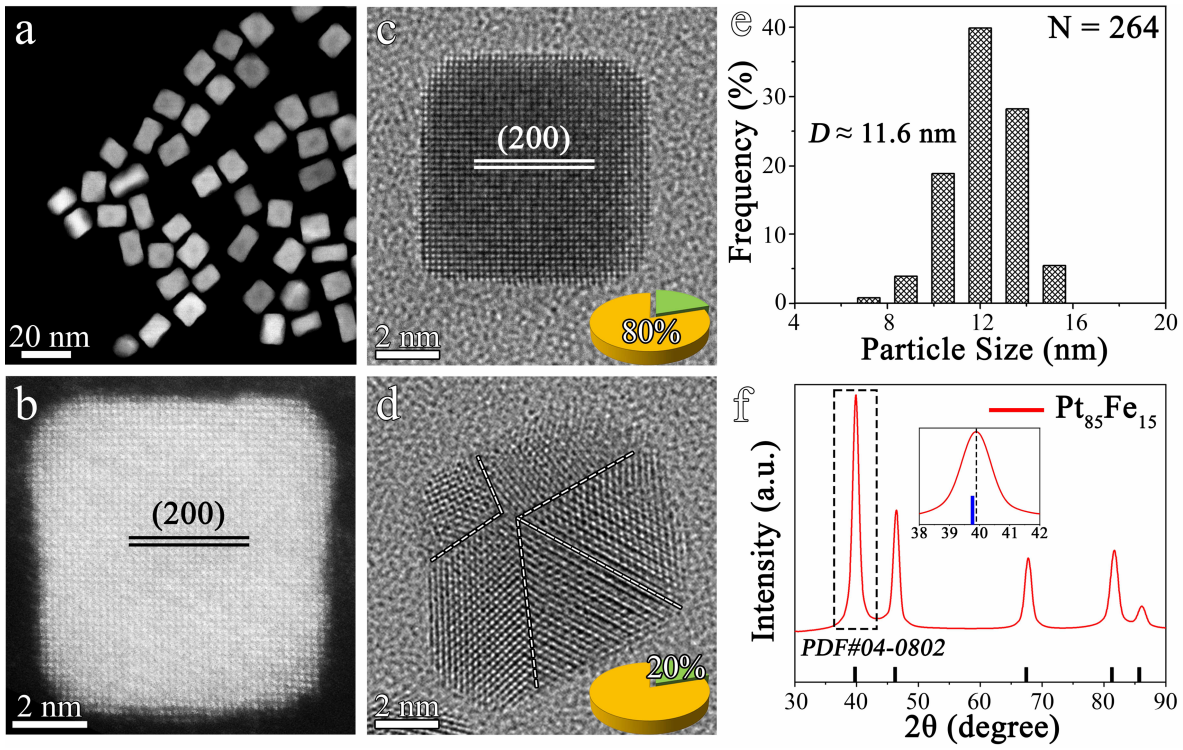

Fig. 1. Characterization of as-synthesized $Pt_{85}Fe_{15}$ NPs. a Low-magnification TEM image showing the well-dispersed NPs. **b** HAADF-STEM image displaying the single-phase, random solid-solution $Pt_{85}Fe_{15}$ alloy. **c, d** HRTEM images showing the representative single-crystal and defective NPs. **e** Particle size distribution of the as-prepared NPs. N indicates the number of included NPs. **f** Synchrotron X-ray diffraction pattern showing the peak shift with a smaller d-spacing of the $Pt_{85}Fe_{15}$ NPs compared to pure Pt. The inset is a zoomed-in view of the (111) peak and its comparison to the peak position (blue line) of Pt(111).

In-situ TEM annealing experiments are then performed to directly monitor the sintering process of $Pt_{85}Fe_{15}$ NPs. Figs. 2a-c present low-magnification TEM images of the same area of well-dispersed $Pt_{85}Fe_{15}$ NPs at room temperature, 400 °C, and 600 °C during vacuum annealing, respectively, at a low electron beam dose rate (790 e/(Å^2 s)). The images illustrate the morphological evolution of individual NPs and the

merging of some closely neighboring NPs (additional examples in Figs. S4) on the ultra-thin carbon support. As indicated by the white arrows in Figs. 2a-c, annealing does not induce obvious particle migration or size changes in the relatively smaller particles. The observation therefore suggests the absence of OR and PMC processes. The bottom panel of Figs. 2a-c provides an enlarged view of three representative regions numbered 1, 2, 3, respectively. In the case of particle 1, its morphology evolves from a nano-cube shape into a round one, driven by the reduction in surface energy through the thermally activated self-diffusion of adatoms along the particle surface. Region 2 shows neck initiation between two closely neighboring NPs at 400 °C, while the three NPs in region 3, with slightly larger inter-particle gaps, undergo neck formation at 600 °C. This indicates that the temperature increase promotes more surface self-diffusion, leading to morphology evolution and facilitating "bridge-like" neck formation at the inter-particle gap region. Additional ex-situ annealing experiments are performed, confirming the neck formation between closely neighboring NPs (Fig. S5).

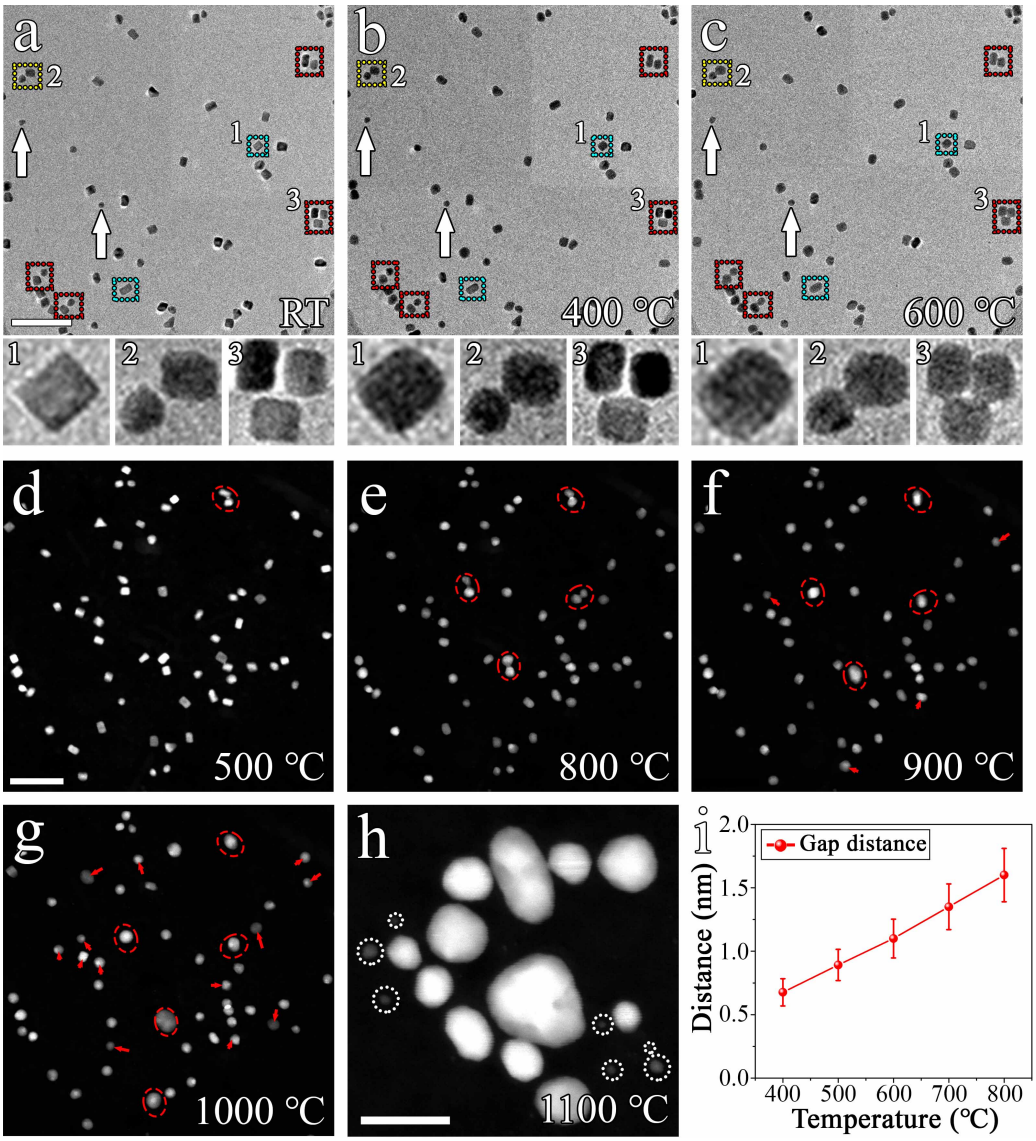

Fig. 2. Low-magnification in-situ TEM/STEM imaging of the morphological evolution and sintering of $Pt_{85}Fe_{15}$ NPs during vacuum annealing. a-c In-situ TEM images revealing the formation of necks between closely neighboring NPs. The bottom panels show an enlarged view of three representative regions marked 1, 2, and 3. **d-g** Time-sequence HAADF images displaying the morphological evolution of NPs as a function of vacuum annealing temperature. The red dashed circles in **e-g** highlight the neck formation between NPs in close neighborhood and their subsequent merging. The red arrows in **f**, **g** indicate the direction and distance of NP migration from their positions shown in **e**. **h** HAADF image showing the shrinkage of small NPs to atomic clusters (marked by white dashed circles), following vacuum annealing at 1100 °C. **i** Inter-particle spacings leading to neck formation at different annealing temperatures. Scale bar, 50 nm **a-g**; 20 nm **h**.

Similar vacuum annealing experiments are also performed with STEM. Figs. 2d-g present in-situ HAADF-STEM images of the same area at different annealing temperatures, using a significantly low electron beam dose rate (72 e/(Å^2 s)). As indicated by the dashed circles in Figs. 2d and 2e, annealing at 500 °C and 800 °C results in neck formation between NPs in the close neighborhood, without inducing significant changes in the particle size or particle migration on the SiN_x support. This is consistent with the in-situ TEM observations in Figs. 2a-c, suggesting the negligible effect of the support on the observed sintering behavior of the $Pt_{85}Fe_{15}$ NPs. Increasing the temperature to 900 °C and above leads to NP migration, as indicated by the red arrows in Figs. 2f, g, where the tails of the arrows represent the positions of the NPs at 800 °C while the heads indicate their new positions at the higher temperature. Sintering becomes more obvious as the temperature is further increased to 1000 °C (Fig. 2g), resulting in both the migration of more NPs and the size shrinkage of smaller particles (additional in-situ STEM observations in Fig. S6). Fig. 2h corresponds to the HAADF image after the temperature is increased to 1100 °C, illustrating the further shrinkage of smaller NPs (marked by dashed white circles), leading to the growth of the larger NPs. The in-situ TEM observations indicate that the sintering behavior of NPs is temperature-dependent. For annealing temperatures below 800 °C, sintering occurs only for closely neighboring NPs, leading to neck initiation via the surface self-diffusion of adatoms on the NPs. The PMC mechanism is activated at 900 °C, as indicated by the observed particle migration. Further temperature increases to 1000 °C and above activate the OR mechanism, evidenced by the size shrinkage of smaller NPs. The inter-particle spacing plays a key role in neck formation between NPs at relatively low temperatures (≤ 800 °C). Fig. 2i shows the measured average inter-particle spacings for neck formation among NPs at annealing temperatures ranging from 400 to 800 °C (with inter-particle spacings measured at room temperature before heating). The results indicate that higher annealing temperatures permit neck formation between NPs at a larger inter-particle gap. This underscores the temperature effect on promoting the morphology evolution of the NPs and facilitating neck formation via surface self-diffusion.

Surface self-diffusion is thermally activated due to the tendency to minimize surface energy, with a higher rate at higher temperatures, regardless of the presence of a neighboring nanoparticle. This process leads to surface morphology fluctuations through the formation and migration of atomic steps around the nanoparticle. Notably, when nanoparticles are in the close proximity, the surface morphology fluctuations contribute to the initiation of neck formation in the inter-particle gap region. Subsequently, self-sustained neck growth occurs through surface self-diffusion. Fig. 3 presents in-situ HRTEM images (with an electron beam dose rate of 8400 e/(Å^2 s)), capturing the atomic-scale process of the surface self-diffusion leading to the neck formation between closely neighboring $Pt_{85}Fe_{15}$ NPs at 500 °C. Fig. 3a presents an HRTEM image of two NPs separated by a visible inter-particle gap, as enclosed within the white dashed box. In this region, one particle exhibits a single-crystalline structure, while the other one is defective with a twin boundary, marked by the red line. Figs. 3b-e depict a time sequence of zoom-in HRTEM images focusing on the inter-particle gap region, revealing the cumulative formation of atomic steps, represented by purple lines. This process arises from surface self-diffusion of adatoms on the facing surfaces of the NPs. Consequently, the inter-particle gap gradually narrows, leading to neck formation through the entrapment of self-diffusing adatoms by the formed atomic steps. As illustrated by the shadowed yellow in Fig. 3e, f, the trapped adatoms continuously self-organize into the crystal lattice that is epitaxial with the single-crystal $Pt_{85}Fe_{15}$ NP. Notably, the neck initiation observed here does not involve the direct collision of the NPs, as suggested by the PMC mechanism. Instead, the initiation of the bridge-like neck formation begins with the trapping of the surface self-diffusing adatoms in the inter-particle gap region.

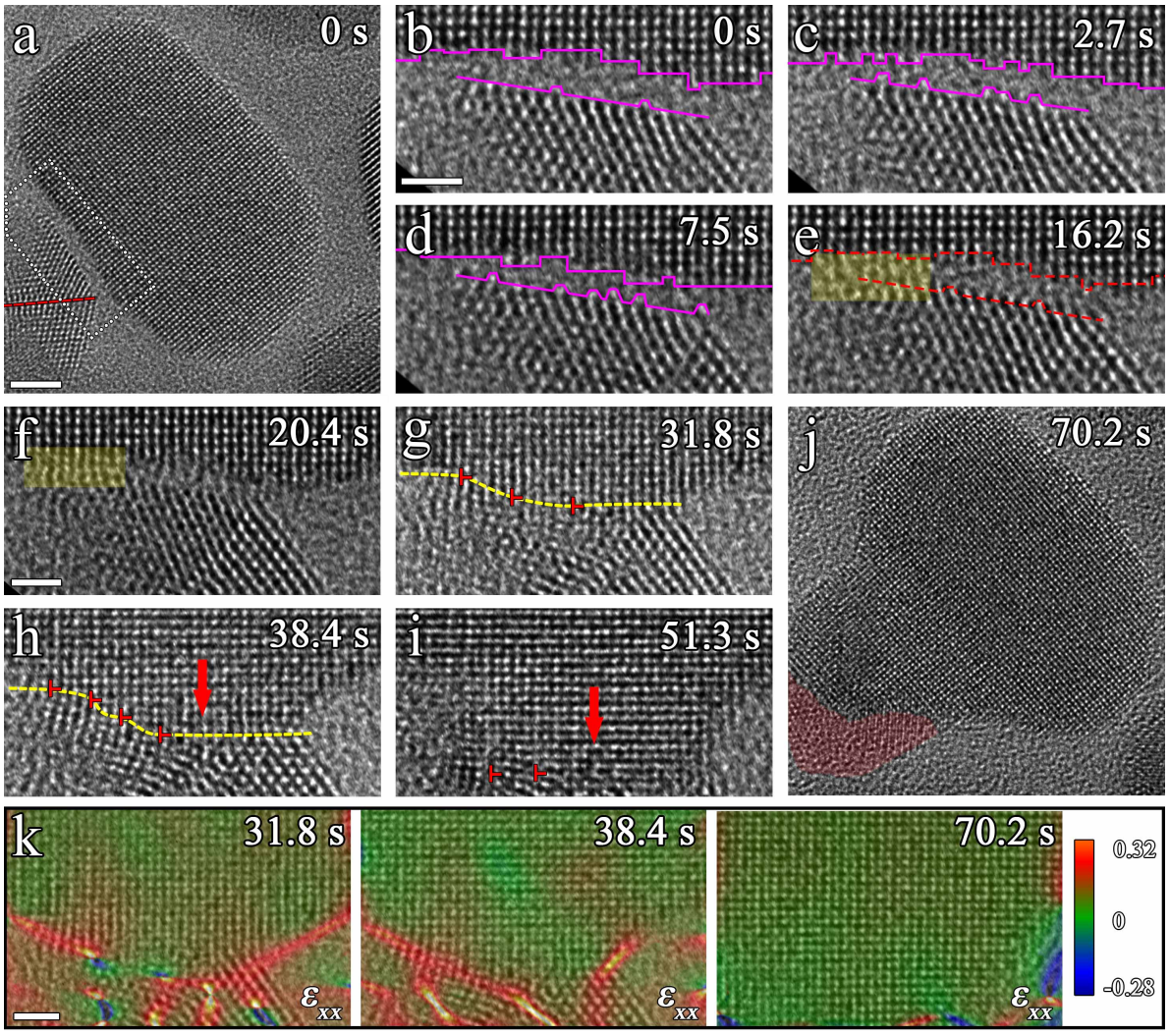

Fig. 3. In-situ HRTEM imaging of the neck formation and growth between $Pt_{85}Fe_{15}$ NPs during the vacuum annealing at 500 °C. a HRTEM image of two closely neighboring NPs, one exhibiting a single-crystalline structure, while the other is defective, including twin boundaries. **b-i** Time-sequence of HRTEM images (Supplementary Movie 1) focusing on the inter-particle gap region, illustrating the trapping of surface self-diffusing adatoms. This process leads to the nucleation and growth of new atomic layers (marked in purple) on both facing facets, facilitating neck formation and growth. The red dashed lines in **e** are the superimposed trace of the position and profile of the facing facets at 0 s in **b**. Red arrows in **h** and **i** indicate the growth direction of the neck toward the defective NP. The red "T" corresponds to edge dislocations at the neck growth front toward the defective NP. **J** HRTEM image of the well sintered NP, showing the conversion of the initially defective NP into the single crystal via the epitaxial growth. The red-marked bottom-left region remains a defective region and has not undergone conversion into the single crystal. **k**

206 Time-sequence HRTEM images with overlapped GPA strain maps (ε_{xx}) of the neck area. Scale bar, 2 nm **a**,
207 **j**; 1 nm **b-k**.
208
209 The sintering process continues with the epitaxial growth of the contacting neck toward the
210 defective NP. This neck growth process involves recrystallization of the defective lattice regions of the NP.
211 This is evidenced by tracking the migration of the growth front of the neck region, forming a low-angle
212 grain boundary mediated by an array of edge dislocations (marked by the yellow dashed lines and red "T"
213 in Fig. 3g-j). The forward propagation of the low-angle grain boundary is accompanied by the retraction
214 motion and rearrangement of the edge dislocations, which requires significant bulk self-diffusion in the
215 defective NP to result in the rearrangement of atoms at the growth front. The epitaxial growth of the necked
216 region is energetically favorable as it results in the annihilation of high-energy structure defects in the
217 defective NP. This is also confirmed by the geometrical phase analysis (GPA) of the time-sequence
218 HRTEM images of the formed neck region in Fig. 3k, demonstrating the decreased strain as the progressive
219 annihilation of high-energy structure defects in the neck region. Fig. 3j provides a relatively lower
220 magnification HRTEM image, illustrating that most of the NP has converted into the single-crystal feature,
221 with the bottom-left region retaining its defective state.
222 The observed neck formation induced by the surface self-diffusion also happens at the inter-particle
223 gap between defect-free NPs. Fig. 4 presents in-situ HRTEM image snapshots of the neck formation
224 dynamics of the nano-cubic $Pt_{85}Fe_{15}$ NPs during the vacuum annealing at 500 °C. The two NPs are defect-
225 free and separated by an inter-particle gap of ~ 1 nm with a face-to-face misalignment of ~ 10.1°, as
226 indicated by the Fast Fourier Transformation (FFT) of the HRTEM image in Fig. 4a. Neck formation is
227 observed to take place by the formation of new atomic layers in the smallest inter-particle gap region (Fig.
228 4b). The newly formed atomic planes grow along the opposing facets of the two NPs, resulting in the
229 formation of a small-angle grain boundary with the presence of several edge dislocations to accommodate
230 their misalignment (marked by red "T" in Fig. 4c). Fig. 4d presents the time sequence of the enlarged views
231 of the inter-particle gap region, showing the atomic process leading to the neck initiation. The thermally

activated surface self-diffusion results in the accumulative trapping of adatoms in the smallest inter-particle gap region (as traced by the purple lines in Fig. 4d), leading to the initiation of the neck formation between the particles. Thereafter, the rearrangement of the trapped adatoms into the epitaxial growth happens on the two closely facing facets (Fig. 4e), where the resulting low-angle grain boundary along with the presence of edge dislocations in the fully merged region also confirms that there is no in-plane rotation of the two NPs during the neck formation process. This lack of in-plane rotation is further supported by the FFTs of the HRTEM images (bottom panel of Figs. 4(a-c)), indicating a consistent misalignment angle between the two equivalent reflections associated with the two NPs throughout the neck formation process. A detailed temporal evolution of the surface morphology for both NPs is presented in Fig. 4f. The surface profiles and positions are compared, revealing a trend toward into a round shape due to thermally activated surface self-diffusion. The accumulative trapping of adatoms at the inter-particle gap leads to the formation of neck contact. Notably, the two single-crystal NPs in contact do not exhibit significant grain growth or shrinkage, distinguishing this behavior from the case depicted in Fig. 3, where the defective NP is consumed through the annihilation of defects in the bulk.

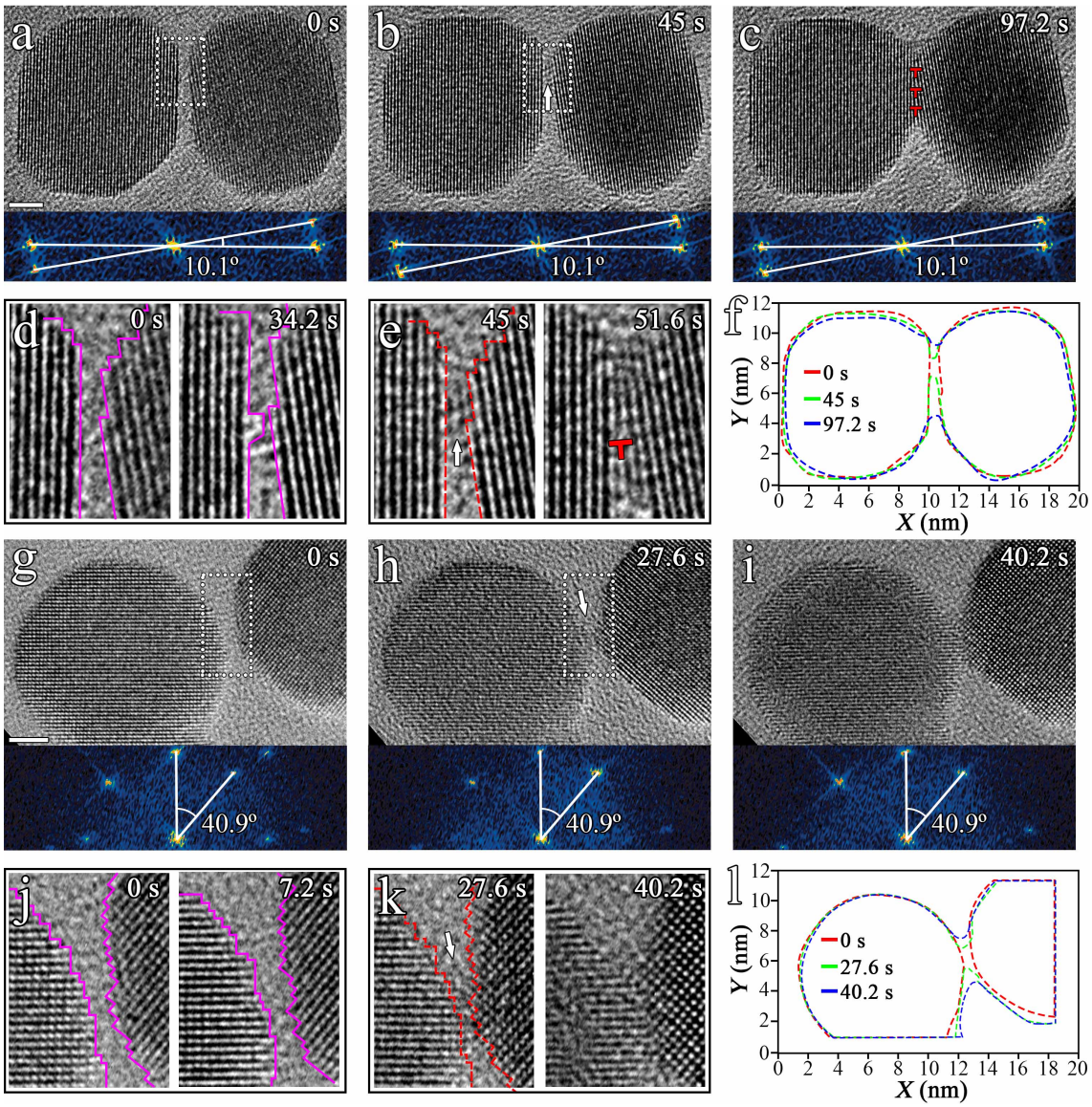

Fig. 4. In-situ HRTEM imaging of the neck formation between single-crystal $Pt_{85}Fe_{15}$ NPs during vacuum annealing at 500 °C. **a-c** Time-sequence HRTEM images (Supplementary Movie 2) showing the neck formation process between the two NPs with slight face-to-face misalignment in the inter-particle gap region. The bottom panel shows the FFTs of the HRTEM images. **d, e** Enlarged views of time-sequence HRTEM images displaying the trapping of self-diffusing adatoms leading to the formation of new atomic layers (marked in purple) on both the facing facets in the inter-particle gap. The red "T" marks the edge dislocations at the low-angle grain boundary. **f** Traces of the morphological evolution of the NPs at different times of the vacuum annealing. **g-i** In-situ HRTEM images (Supplementary Movie 3) illustrating the sintering process of two NPs with the facing vertices in the inter-particle gap region. The bottom panel shows the FFTs of the HRTEM images. **j, k** Enlarged views of the time-sequence HRTEM

images showing the extension of the lattice planes (marked in purple) on both the facing facets by the trapping of self-diffusing adatoms in the inter-particle gap. The red dashed lines in **e** and **k** are the superimposed traces of the position and profile of the facing facets at 0 s in **d** and **j**, respectively. **l** Traces of the morphological evolution of the NPs in (g-i) at different annealing times. Scale bar, 2 nm **a-c**, **g-i.**

Figs. 4g-i present in-situ HRTEM imaging of the corner-to-corner neck formation between two defect-free NPs featuring a large in-plane misorientation angle. The FFT of the HRTEM image (bottom panel in Fig. 4(g)) confirms that both NPs are along the [100] zone axis but have an in-plane rotation (misorientation) angle of ~ 40.9º. As observed in Figs. 4g, i, the neck formation occurs in the corner-to-corner region that has the shortest inter-particle gap of ~ 1 nm, resulting in a high-angle grain boundary in the merged region. The FFT of the HRTEM images in Fig. 4g-i show the in-plane misorientation angle between the NPs remains unchanged at 40.9º, confirming that there is no particle rotation during the neck formation process. Fig. 4j depicts the time-sequence, enlarged views of the corner-to-corner region marked by the white dashed rectangle in Fig. 4g, showing independent growth of lattice planes of the facing facets of the two NPs, thereby resulting in a merged high-angle grain boundary (Fig. 4k). Detailed tracing of the surface morphology evolution of the two NPs is depicted in Fig. 4l, showing the corner rounding by the surface self-diffusion to result in the mass transfer to the neck region. Additional examples of the morphology evolution of the $Pt_{85}Fe_{15}$ NPs, leading to the inter-particle neck and formation of various grain boundaries during surface self-diffusion-induced sintering, are presented in Figs. S7.

The in-situ HRTEM imaging of the neck region shown in Figs. 3 and 4 demonstrates that the neck formation occurs via the nucleation and growth of new atomic layers on the two facing facets of the adjacent NPs as a result of the trapping of surface self-diffusing atoms in the inter-particle gap region. This contrasts with the OR process, where the anticipated outcome involves the shrinkage (involving atomic evaporation and/or detachment) of atomic layers on one facing facet and the nucleation/growth of new atomic layers on the opposite facing facet due to the net mass transfer from the small particle to the larger one. The absence of the OR process is also corroborated by the low-magnification TEM and STEM imaging in Fig. 2,

showing negligible changes in particle sizes, even for the smallest particles for the annealing at the relatively lower temperature (≤ 600 °C). This suggests that the neck formation does not involve long-range diffusion of atoms evaporating or detaching from smaller particles that are not within the close vicinity.

The in-situ TEM observations shown above are performed with $Pt_{85}Fe_{15}$ NPs that tend to develop into the Pt_3Fe $L1_2$ ordered phase upon the vacuum annealing, as confirmed from our HAADF-STEM imaging (Fig. S7). For comparison, in-situ STEM imaging of the sintering behavior of $Pt_{65}Fe_{35}$ NPs is also performed. As shown in Fig. 5(a-c), the vacuum annealing of $Pt_{65}Fe_{35}$ NPs results in the neck formation among closely neighbored NPs without significant changes in particle size and migration, similar to the $Pt_{85}Fe_{15}$ NPs (Fig. 2). Atomic-scale HAADF-STEM images show that the vacuum annealing results in the PtFe $L1_0$ ordering for $Pt_{65}Fe_{35}$ NPs (Figs. 5(d-i)) and the Pt_3Fe $L1_2$ ordering for $Pt_{85}Fe_{15}$ NPs (Fig. S7) without obvious elemental surface segregation. The HAADF images of sintered $Pt_{65}Fe_{35}$ NPs also show the formation of various microstructure features, including perfect lattice matching (Figs. 5(d, g)), and small-angle grain boundary (Figs. 5(e, h)) and high-angle grain boundary (Figs. 5(f, i)) in the neck region, akin to observations from the sintering of $Pt_{85}Fe_{15}$ NPs (Figs. 3 and 4). The small-angle grain boundary consists of discrete dislocations, marked by the red 'T' in Fig. 5h, whereas the high-angle grain boundary is formed between grains with a misorientation of 34° as shown in Fig. 5i. It is worth noting that Pt_3Fe $L1_2$ and PtFe $L1_0$ ordered phases have Curie temperatures of approximately 70 °C and 400 °C, respectively.[39,40] Beyond these Curie temperatures, the NPs lose their magnetic properties. Given that our in-situ TEM imaging was conducted at temperatures exceeding 400 °C, it is evident that the sintering observed is not attributable to the magnetic attraction-induced motion of the NPs. Instead, the observed neck formation induced by surface self-diffusion is dependent on the initial inter-nanoparticle gap. This gap is significantly influenced by the dispersion of the NPs during the drop-cast process.

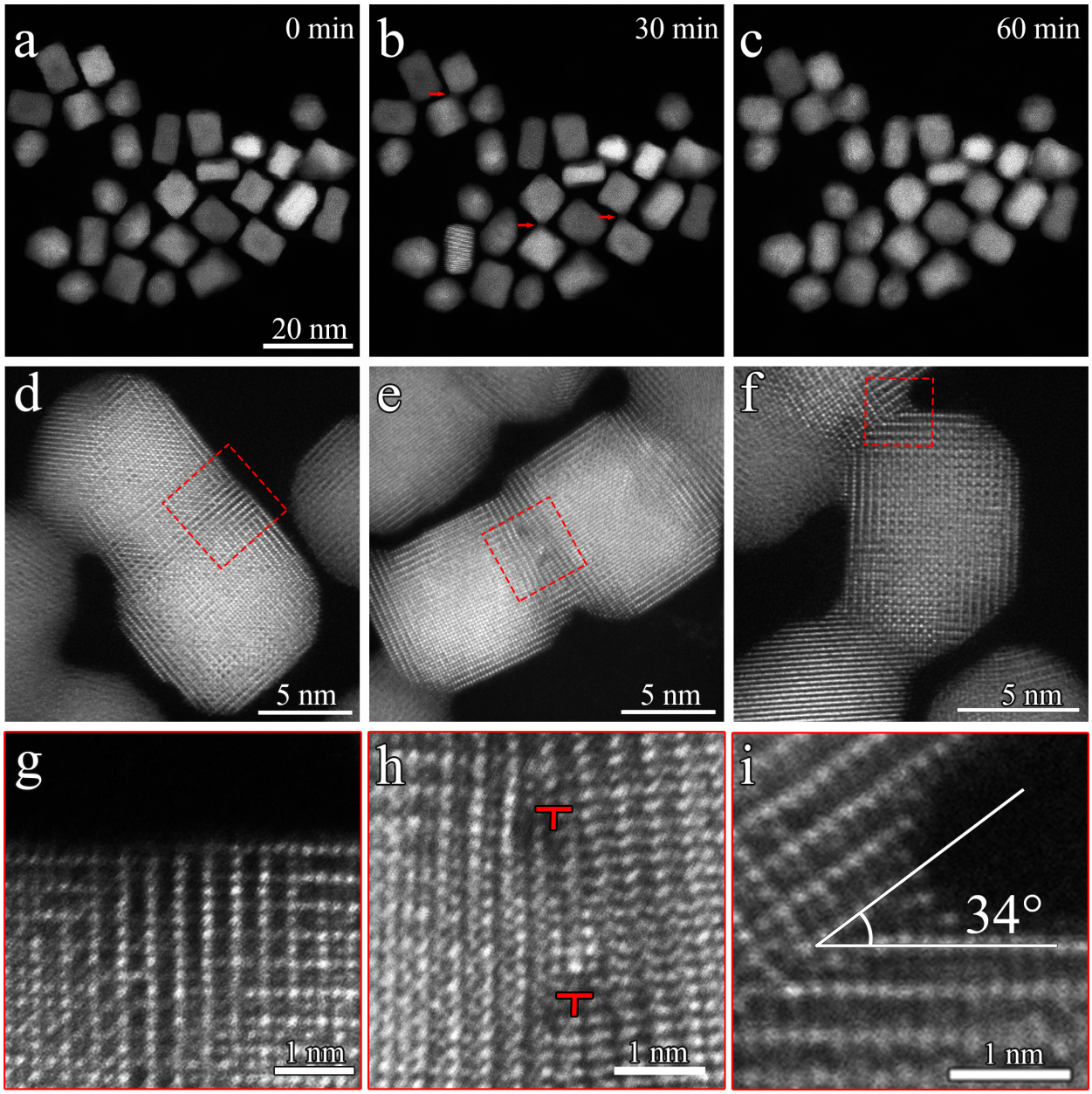

Fig. 5. HAADF-STEM imaging of the sintering of $Pt_{65}Fe_{35}$ NPs under vacuum annealing at 600 °C. a-c Time-sequenced HAADF images showing the contacting neck formation among the NPs in the close neighborhood. **d-h** HAADF images showing the perfect merging of the lattice planes, low-angle, and high-angle grain boundaries in the neck region. Red "T" marks discrete dislocations within the low-angle grain boundary. **g-i** Zoomed-in HAADF images of the neck regions marked by the red dashed boxes in (**d-f**), respectively.

When conducting in-situ TEM observations (Figs. 2-5), it is essential to carefully assess potential effects from the electron beam irradiation, including radiolysis, atomic displacement and local heating, on the sintering dynamics of NPs. Following established procedures,[8,10,20] we performed thorough evaluation of electron beam effects through "blank-beam" and controlled electron dose experiments. As depicted in Figs. 6(a-c), real-time HRTEM images demonstrate the high stability and negligible morphology changes of $Pt_{85}Fe_{15}$ NPs under continuous electron beam irradiation at a dose rate of 11200 e/(Å²·s) at room temperature. This dose rate exceeds that used in the in-situ HRTEM observations shown in Figs. 3 and 4. These findings confirm the occurrence of thermally activated surface self-diffusion, leading to the observed rounding tendency of NPs at elevated temperatures. Furthermore, we evaluated the potential effects of electron beam irradiation by comparing the sintering dynamics of Pt-Fe NPs exposed to the beam with those that were not. The electron beam was unblanked for only a few seconds to capture time-sequenced HRTEM and temperature-sequenced HAADF snapshots at the beginning and end of the sintering experiments, minimizing e-beam exposure during imaging. Figs. 6(d-f) show the HAADF images of the NPs at room temperature and after vacuum annealing to 500°C, illustrating the formation of necks between the NPs during electron beam blanking.

Similarly, Figs. 6(g-i) and 6(j-l) present HRTEM image snapshots from two distinct vacuum annealing experiments of NPs under the blanked electron beam. They illustrate neck formation within the interparticle gap region – one due to the encounter of growing perpendicular lattice planes, and the other due to slightly misaligned merging of the lattice planes, respectively. The zoomed-in views of the inter-particle gap in Figs. 6(g-l) reveal that neck formation occurs through the nucleation and growth of new atomic layers on the two opposing surfaces of the NPs. Concurrently, other surface regions of the NPs experience gradual mass loss, as indicated by the purple markings in Figs. 6(h, i, k, l). This correlation suggests that mass is transferred from these recessed surface areas to the inter-particle gap via the surface self-diffusion, thereby facilitating neck formation. The observed necking formation under the blanked electron beam (alongside additional examples in Figs. 5(a-c), S4 and S5) aligns consistently with in-situ

observations depicted in Figs. 3 and 4. Furthermore, the low-magnification in-situ observations shown in Figs. 2(a-c), which involved significantly lower electron beam doses, illustrate morphology evolution and subsequent NP sintering, corroborating well with the HRTEM observations. These findings further confirm the minimal impacts of electron beam irradiation on the sintering dynamics in our study.

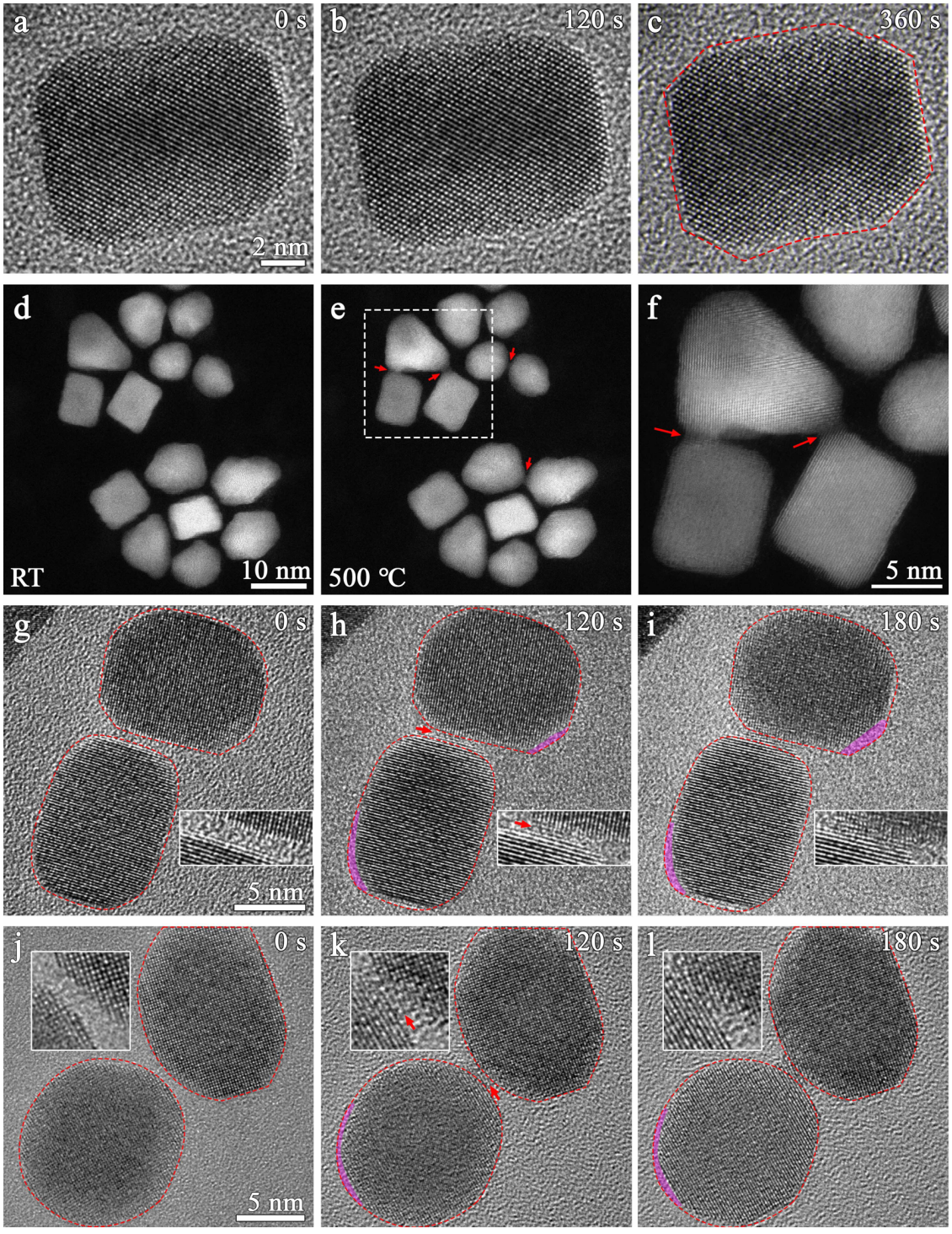

Fig. 6. Evaluation of electron beam irradiation effects on sintering dynamics of Pt-Fe NPs. a-c Time-sequence HRTEM images demonstrating negligible effects of electron beam irradiation on $Pt_{85}Fe_{15}$ NPs at room temperature. The red dashed line in **c** represents the superimposed traces of the position and profile of the surface at 0 s. **d**, **e** HAADF images displaying the as-dispersed $Pt_{85}Fe_{15}$ NPs and after vacuum annealing to 500 °C with the electron beam blanked. **f** Zoomed-in HAADF image of the region marked by the white dashed box in (**e**), showing the neck formation in the inter-particle gap regions. **g-i** Time-sequence HRTEM images depicting neck formation through the encounter of growing perpendicular lattice planes in the inter-particle gap region during vacuum annealing at 500 ℃ with the electron beam blanked. **j-l** Time-sequence HRTEM images illustrating neck formation via merging of growing slightly misaligned lattice planes of neighboring NPs during vacuum annealing at 500 ℃ with the electron beam blanked. The electron beam was unblanked for ~ 1 s to capture image shots in (**g-l)**. Red arrows in (**e-l)** highlight the neck formation. The insets in (g-l) are zoomed-in views of the inter-particle gap regions. The red dashed lines in (g-l) track the position and profile of the NP surface at 0 s. The regions marked by purple indicate mass loss associated with neck formation in the inter-particle gap.

Atomistic simulations are then performed to further elucidate the microscopic processes underlying the experimentally observed neck formation. We first examine the stability and mobility of surface atoms using first-principles calculations based on density functional theory (DFT). The calculated energies for the complete detachment of an atom from the flat surfaces (to form free atoms) are ~ 5.95 eV for (100) and ~ 4.6 eV for (111). These values are significantly larger than the barriers for surface self-diffusion, which are ~ 1.08 eV for (100) and ~ 0.60 eV for (111)) (more details in Fig. S8). The substantial difference in the activation energies suggests that the surface self-diffusion-induced neck formation is kinetically more favorable and can be activated at a relatively lower temperature than the OR process that requires complete detachment (evaporation) of atoms from the NPs.

Molecular dynamics (MD) simulations are then performed to elucidate the kinetic process of the neck formation. Due to the large time-scale gap between experiments and MD simulations, a higher annealing temperature of 1473 K is used to accelerate the MD simulations for better comparisons with the experiments. Fig. 7(a) illustrates the structure model for the MD simulations, where the two NPs are

separated by an inter-particle gap of ~ 5.5 Å (larger than the interaction cutoff distance of ~ 4 Å) between the two facing facets. Figs. 7(b-g) capture the temporal evolution of the inter-particle gap region in Fig. 7(a). Consistent with the DFT prediction, the vacuum annealing does not induce evaporation of atoms from the NPs, instead, it drives surface self-diffusion of adatoms as a result of the tendency toward the rounding of the crystal facets of the NPs. As marked in black, blue, and purple, respectively, in Figs. 6(b-g), the path trajectories for three representative adatoms are also traced to observe the surface self-diffusion of the surface adatoms that results in their trapping at the inter-particle gap. The MD simulation snapshots visually depict the sequence of events culminating in the reduction of the inter-particle gap. This reduction is driven by the self-diffusion of adatoms to the inter-particle gap region, where they form single atomic steps (as marked by the red arrows in Fig. 7(c, d)), subsequently trapping additional self-diffusing adatoms and ultimately triggering neck formation. It is noteworthy that while surface morphology fluctuations also occur at other surface facets, these fluctuations can quickly dissipate in the absence of neighboring NPs in close proximity.

The MD simulations match well with the experimentally observed neck initiation and growth (Figs. 3, 4). To further confirm the atomic clustering-induced sintering, the time evolution of the center of mass (COM) of the two NP system is followed using the MD simulation outcomes. As shown in Fig. 7(h), the COM remains almost un-displaced throughout the merging process, confirming the absence of any mass loss or mass transfer from one NP to the other one. This happens because no external forces act on the two NPs, and the neck formation and growth are simply induced by the trapping of surface self-diffusing adatoms in the inter-particle gap region. To further evaluate the temperature and inter-particle distance effects, our MD simulations of annealing at the lower temperatures of 1073 K and 1273 K and a larger inter-particle gap of 1 nm do not yield noticeable neck formation (Figs. S9 and S10). This is consistent with the in-situ TEM and STEM results (Fig. 2) of the sufficiently high temperature and small inter-particle distance required for the neck formation.

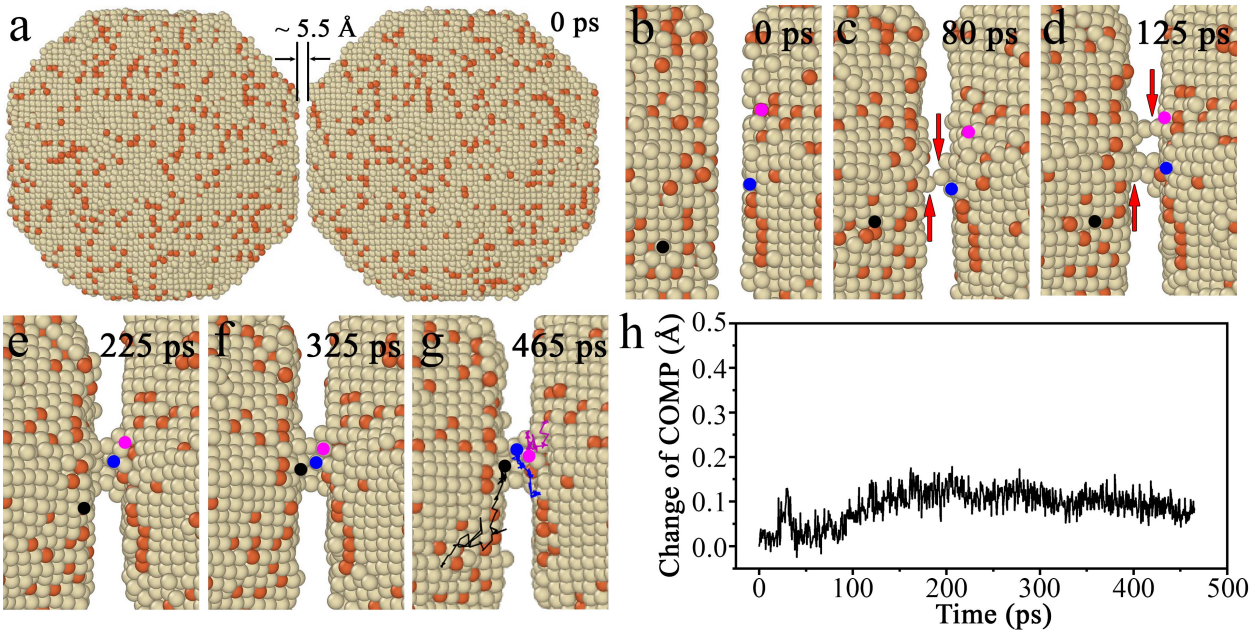

Fig. 7. MD simulations of the neck dynamics during vacuum annealing at 1473 K. a Structure model of two $Pt_{85}Fe_{15}$ NPs separated by 5.5 Å of the inter-particle gap. **b-g** Snapshots of the inter-particle gap region, showing the nucleation and growth of new atomic layers on the two facing facets by surface self-diffusing adatoms in the inter-particle gap region. The black, blue, and red lines correspond to the surface diffusion trajectories of the three adatoms marked in black, blue, and purple, respectively. **h** COM of the two NP system measured as a function of the simulation time.

The in-situ TEM and STEM observations indicate the negligible effect of the SiN_x and carbon support on the sintering behavior of the Fe-Pt NPs as a result of the surface self-diffusion process. However, it is worth mentioning that both the carbon and SiN_x are considered inert supports that do not interact strongly with the supported metal. By contrast, reducible oxide supports (such as ZnO, TiO_2) are known to interact strongly with supported metal to result in the encapsulation of the metal by a reduced thin oxide layer migrating from the oxide support,[41,42] for which the surface self-diffusion of the NPs can be effectively suppressed. Therefore, the nanoparticle-support systems with the strong metal-support interaction (SMSI) effect are not expected to exhibit the sintering behavior as a result of the surface self-diffusion for the pristine NPs as shown above.

The driving force for the sintering of NPs is to reduce the overall surface energy of an ensemble of NPs. However, this global energy consideration does not adequately account for the changes in the free energy landscape of individual NPs and how these changes influence the specific sintering pathways such as the classic OR and PMC processes. In contrast, our in-situ TEM observations and atomistic simulations reveal that the tendency to assume a round shape to decrease the surface area of a single NP induces significant surface self-diffusion. This rounding propensity is further illustrated by the low-magnification in-situ STEM imaging conducted at a low electron beam dose rate (34 e/($Å^2$ s)) (Fig. 8(a-c)), where the NPs are exposed to the electron beam only during image capture (i.e., the beam is blanked for most of the annealing process). The NPs, whether far apart or closely neighbored, exhibit notable morphological changes. Similarly, the in-situ HRTEM image snapshots, acquired with the electron beam unblanked for ~ 1s at a dose rate of 5420 e/($Å^2$ s), further demonstrate the morphological evolution while minimizing electron beam exposure (Figs. 8(d-f)). This is evidenced by the observed growth along certain surface regions, accompanied by mass transfer from receding surface regions (Figs. 8(d-f)). Such morphological evolution involves surface self-diffusion, which in turn, facilitates the initiation of neck formation at inter-particle gaps for closely neighboring NPs.

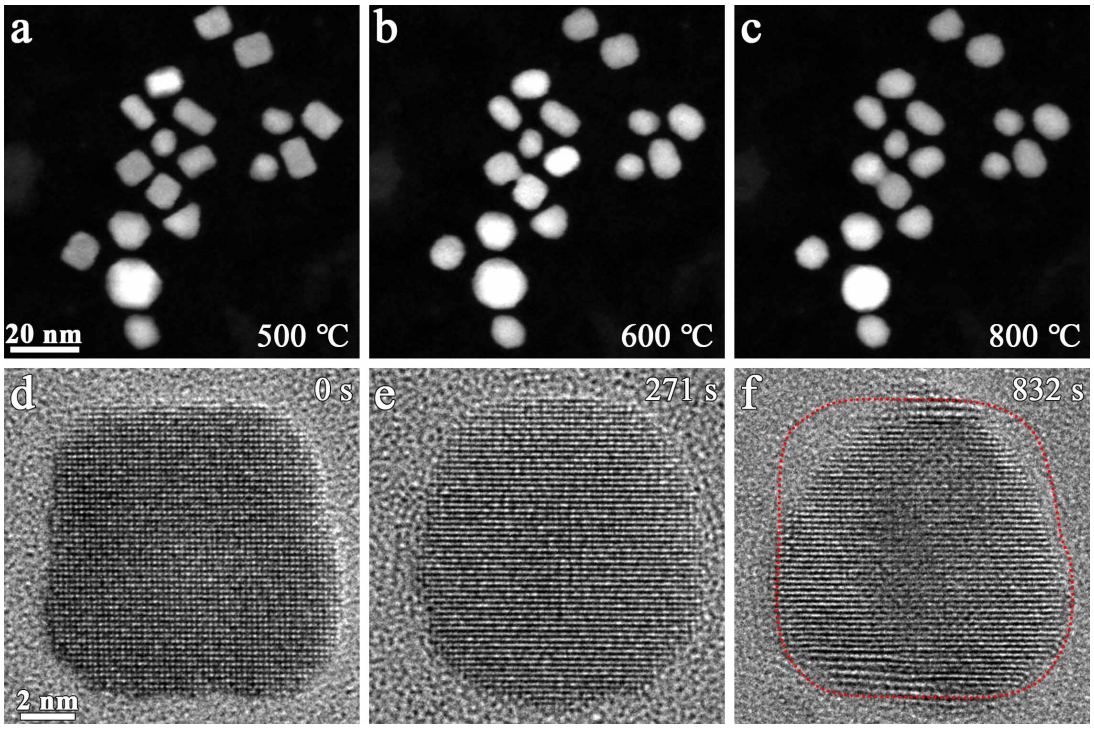

Fig. 8. In-situ STEM and HRTEM imaging of the morphological evolution of annealed Pt-Fe NPs. a-c, Time-sequence of low-magnification STEM-HAADF images showing the rounding tendency of $Pt_{85}Fe_{15}$ NPs. **d-f**, HRTEM images depicting growth along certain surface regions with mass transfer from the receding surface regions of an $Pt_{65}Fe_{35}$ NP annealed at 600 ℃. The red dashed line in **f** represents the superimposed trace of the position and profile of the NP surface at 0 s. The electron beam was only unblanked to capture image shots.

Discussion

The necking phenomenon described above is based on shape-controlled Pt-Fe nano-cubes by taking advantage of their faceted surfaces and relatively uniform size distribution. These nano-cubes exhibit promising catalytic properties for oxygen reduction reaction (ORR) in electrocatalysis.[1] Ordered Pt-M NPs (where M = Fe, Ti, Cu, Co, etc.) have garnered significant interest due to their high stability and reactivity in ORR.[1,34,35] Thermal annealing is a crucial step for achieving the ordered intermetallic phase and for controlling the shape and surface structure, both of which are vital for enhancing electrocatalytic performance. Therefore, a comprehensive understanding of the evolution of size, structure, and morphology during thermal annealing is essential for optimizing catalytic efficiency. The insights gained from in-situ

TEM imaging of the necking phenomenon offer practical implications for manipulating the morphology, size distribution, and stability of NPs by leveraging surface self-diffusion processes.

It is crucial to clarify any potential effects of electron beam irradiation on the outcomes of our in-situ TEM experiments. The e-beam dosing rate employed in our in-situ STEM/TEM imaging is significantly higher than that used by Bredmose et al.,[17] but comparable to that of Song et al.[19] Our thorough evaluation, which includes "blank-beam" and varying electron dose rates (Figs. 6, S4, S5 and S7), confirms that the higher electron beam dose rates used in our experiments do not produce noticeable effects on the sintering behavior of the Fe-Pt nanoparticles. Several factors contribute to the enhanced stability of the nanoparticles against e-beam irradiation during our in-situ TEM experiments: 1) large particle sizes – the particle sizes used in our experiments exceed ~ 11 nm, which is considerably larger than those (~ 3 nm or smaller) typically used in other in-situ TEM studies; 2) alloying – Fe-Pt alloys exhibit a strong ordering tendency (as illustrated in Fig. 5), leading to superior atomic bonding compared to pure metals utilized in other research. This strong atomic arrangement enhances the stability and resistance of the NPs against electron beam bombardment and sputtering. Consequently, Fe-Pt NPs are more resistant to changes induced by high-energy electron exposure, which is crucial for in-situ TEM imaging.

In comparing data acquisition in TEM and STEM modes, the focused e-beam in STEM allows for lower exposure at each point, as the beam is rapidly scanned across the specimen. Additionally, our in-situ STEM observations prioritize low-magnification imaging (Figs. 2, 5, 8(a-c)), which further decreases the electron dose rate. In contrast, the broader electron beam used in in-situ HRTEM imaging can lead to higher overall electron doses over larger areas of the specimen. However, a comparison of our in-situ HRTEM imaging results (Figs. 2, 3, 8(d-f)) with “blank-beam” HRTEM imaging (Figs. 6(g-l)) demonstrates similar neck formation behavior. This consistency confirms that the electron dose rate during the in-situ HRTEM imaging remains within a safe range, preventing any artifacts that could affect the sintering behavior of the NPs.

The observed initiation of neck formation resulting from surface self-diffusion is therefore an intrinsic behavior for closely neighboring NPs. This can happen particularly in high loading catalyst

scenarios where NPs are in close proximity. The surface self-diffusion mechanism is also relevant to the PMC process, which relies on Brownian-like motion of NPs to bring NPs into proximity. However, the microscopic mechanism for neck initiation is not fully explained by the conventional understanding of the PMC process. As shown above, the arrest of surface self-diffusing atoms at the inter-particle gaps works as the atomic origin of the neck initiation between closely neighboring NPs. Our in-situ TEM observations (Fig. 2) further demonstrate that the neck initiation through surface self-diffusion is activated at a lower temperature than the OR and PMC processes. The lower activation energy for surface self-diffusion compared to atomic evaporation and particle migration contributes to this temperature dependency. The study suggests that inhibiting surface self-diffusion, either by increasing activation energies or through the SMSI effect, can effectively hinder the neck formation and thus prevent the NPs from sintering at elevated temperatures.

Surface self-diffusion in the sintering of NPs has been previously described by Schested et al. as a mechanism responsible for both particle migration and coalescence.[27] However, a key distinction in our observations is the absence of net particle migration. Our in-situ TEM imaging (Figs. 2, 4, 5, 6, 8) indicates that the drive to minimize the surface energy of individual particles results in significant surface self-diffusion of atoms, leading to a more rounded shape without inducing noticeable migration of the NPs. This lack of particle migration is further corroborated by our MD simulations, which show no change in the center of mass of the particles (Fig. 7). This absence of migration can be attributed to the limited inter-particle interactions among NPs of similar sizes. The kinetic entrapment of surface self-diffusing atoms in the gaps between closely spaced NPs facilitates neck formation, allowing for coalescence without need for significant particle movement.

The sintering mechanism observed in our case, driven by surface morphology evolution induced by self-diffusing adatoms, also contrasts with the process of oriented attachment,[43–45] which involves the migration and alignment of crystallographic planes. The absence of the need for migration and rotation of NPs for crystallographic alignment in our scenario is highlighted by the formation of low-angle and high-angle grain boundaries in the merged NPs shown in Figs. 4 and 5. Nevertheless, the neck growth toward

the highly defective region of the merging nanoparticle leading to a single-crystal nature, as depicted in Fig. 3, shares the common driving force with oriented attachment in terms of minimizing interface energy.

Our in-situ TEM imaging and MD simulations reveal that the necking mechanism via surface self-diffusion requires close proximity between NPs. Several processes can promote this proximity: 1) high catalyst loading – increased catalyst loading increases the surface density of NPs on the support, enhancing the likelihood of NPs being in close proximity. This high density fosters effective interactions that promote neck formation and subsequent sintering. 2) Thermally driven Brownian migration – the random movement of NPs due to thermal energy can draw NPs closer together, facilitating neck formation through surface self-diffusion even before the NPs make physical contact.

Minimizing the surface free energy is the driving force for influencing the sintering behaviors of nano catalysts. As well-documented in previous studies,[10,11,13,20,46,47] the sintering by atomic evaporation into the vacuum or diffusion across the substrate surface usually depends on the particle size. Specifically, smaller particle sizes result in higher Laplace pressure for atomic evaporation or detachment. However, in our study, the NPs have a relatively large size (> 10 nm), where the surface self-diffusion becomes more readily activated compared to atomic evaporation, playing a key role in controlling the sintering behavior of the NPs. The fundamental insights shown above could have broader applicability for the stability design of nano-catalysts. The co-selection of a suitable size (~ 10 nm) and loading (inter-particle distance > 1 nm) can be the strategy to achieve a balance between activity and stability in nano-catalysts. This approach aims to prevent excessive sintering by promoting stable inter-particle distances and optimizing the overall performance of the catalyst.

Conclusions

In conclusion, the study reveals a sintering phenomenon by which NPs merge through the trapping of surface self-diffusing adatoms in the inter-particle gap region. This process is driven by the thermally driven rounding of the crystal facets of the NPs, promoting the flux of self-diffusion of adatoms on the NP surfaces. The entrapment of self-diffusing adatoms in the narrow inter-particle gap results in a higher concentration of adatoms, facilitating collision interactions for the nucleation and growth of new atomic layers, leading to neck formation between NPs. Importantly, this surface self-diffusion-driven sintering process is activated at a relatively lower temperature compared to other sintering mechanisms such as OR and PMC. The fundamental insights shown here are of wide relevance and considerable practical importance for manipulating the morphology, size distribution, and stability of nanostructures using surface self-diffusion processes.

Experimental and modeling methods

Synthesis of Pt-Fe solid-solution alloy nanoparticles. Pt-Fe cubic NPs were prepared using a modified method reported previously.[48] Typically, for the synthesis of the $Pt_{85}Fe_{15}$ NPs, 0.05 mmol $Pt(acac)_2$ (≥ 99.9%, Alfa Aesar) and 0.05 mmol $FeCl_2 \cdot 4H_2O$ (98%, Alfa, Aesar) were dissolved in 5.0 mL of octadecene (ODE, 90%, Sigma-Aldrich), 4.0 mL of oleylamine (OAm, 70%, Sigma-Aldrich) and 1.0 mL of oleic acid (OA, 90%, Sigma-Aldrich) in a 100 mL three-neck flask. The mixture was degassed under vacuum at 100 °C for 1 hour to eliminate moisture and oxygen. Under Ar protection, the transparent yellowish solution was gradually heated to 130 °C for 3 min, followed by rapid addition of 0.050 g of $W(CO)_6$ (97%, Sigma-Aldrich). The system was then sealed tightly, and the temperature was raised to 230 °C within 15 min and held constant for 30 min. Subsequently, the flask was gradually cooled to room temperature using air blowing, and the resulting products were purified through multiple cycles with 30.0 mL mixture of hexane and ethanol in a 1:1 ratio. The Pt-Fe NPs were collected through centrifugation and ultimately redispersed in hexane to achieve a uniform suspension.

To mitigate the potential impact of surface contamination on sintering behavior, several precautionary steps were implemented in our experiments. A solution of 0.1 M NaOH (98%, Alfa Aesar) in anhydrous ethanol was utilized to thoroughly wash the PtFe NPs multiple times, effectively eliminating most residual organic ligands covering the surface. Subsequently, the NPs underwent plasma treatment before being loaded into the TEM for vacuum annealing. This annealing process served to decompose and eliminate any remaining organic residues. As indicated by HRTEM images (Figs. 3, 4) and atomic-scale HAADF images (Figs. 5 and S7), the annealed NPs exhibit pristine surfaces without any noticeable capping layer.

Materials Characterization. To investigate potential support-induced effects on the sintering behavior of Pt-Fe NPs, the as-prepared Pt-Fe NPs, subjected to 5 min of ultrasonication, were drop-cast onto SiN_x and carbon films, respectively. In-situ TEM experiments were conducted using a DENSsolution heating holder and a Gatan heating holder in an environmental TEM (FEI Titan 80-300) equipped with an objective-lens aberration corrector. The Gatan Orius SC1000 (model 832) CCD camera was used to capture in-situ HRTEM videos at a frame rate of 14 fps. The annealing processes were carried out with a heating rate set at 100 °C /min, and each temperature stage included a 1-minute hold to minimize thermal drift before TEM observation. To mitigate potential electron beam-induced artifacts, the sample underwent exposure to the e-beam solely during the acquisition of low-magnification TEM and STEM images. Additionally, the sintering experiment was replicated with a complete blanking of the electron beam

during vacuum annealing, and HAADF images of sintered NPs were subsequently captured at room temperature. The high melting temperature (~ 1500 °C) of the Fe-Pt alloy and the relatively large particle size (> 10 nm) of the Fe-Pt NPs in our work contribute to minimizing any potential electron-beam induced damage. In-situ HRTEM movies were captured to monitor structural and morphological evolution of the NPs during the annealing processes. Additionally, in-situ HAADF-STEM imaging of NPs sintering at low magnification was performed with FEI Talos. Ex-situ HAADF-STEM imaging was performed using a probe-corrected STEM (Hitachi 2700).

Atomistic simulation. MD simulations of the sintering of $Pt_{85}Fe_{15}$ NPs were performed using the LAMMPS package.[49] The modified embedded atom method (MEAM) potential developed by Kim et al. was employed to describe the interatomic interactions.[50] The initial atomic configurations of the NPs were generated through the Wulff construction method using the Wulff Pack code.[51] To simulate the surface self-diffusion of adatoms at high temperature, a monolayer of atoms was initially introduced on the opposing (100) facets of two adjacent NPs. Subsequently, 80% of the surface atoms were randomly removed to generate a configuration with adatoms randomly distributed on the facets. The constructed NP consisted of a total of 30802 atoms, with 4620 Fe atoms distributed randomly, achieving an overall composition close to the experimental ratio ($Pt_{85}Fe_{15}$). Prior to the sintering simulation, individual NPs underwent isothermal equilibration at 1473 K for 465 ps in the canonical ensemble (NVT). After the removal of the angular momentum, two NPs with the equilibrated structures were positioned within a single box, aligning the (100) facet of one NP in parallel to the facing (100) facet of the other NP, with a separation distance of 5.5 Å. Visualization of simulation snapshots at various time points was caried out using the OVITO software.[51] To assess the temperature effect on neck initiation, MD simulations were also conducted at lower temperatures of 1073 K and 1273 K for 465 ps, providing comparative insights.

The energy for atomic detachment and the barrier for self-diffusion of a Pt adatom on the (001) and (111) surfaces of a $Pt_{85}Fe_{15}$ alloy were predicted through first-principles calculations using DFT. The calculations were performed using the Vienna Ab initio Simulation Package (VASP).[52] The projector-augmented wave (PAW) method was used with an energy cutoff of plane wave at 500 eV.[53] The exchange-correlation interactions were described by the generalized gradient approximation (GGA) using the Perdew, Burke, and Ernzerhof (PBE) functional.[54] Brillouin zone integration was performed using the first-order Methfessel-Paxton method with a smearing width of 0.2 eV. The convergence criterion of the electronic self-consistent loop was set as 10^{-6} eV. Co-linear spin alignment was enabled in the calculations to account for the possible ferromagnetic feature of a $Pt_{85}Fe_{15}$ alloy. The calculation supercell for

579 the bulk alloy adopted a special quasi-random structure (SQS) generated by the ATAT code[55,56] to mimic the random
580 mixing of Fe and Pt atoms in an fcc lattice. Following full relaxation, a vacuum layer of 15 Å was introduced along
581 the c-axis of the bulk alloy supercell to create free surfaces of the (001) and (111) planes. The structure with free
582 surfaces underwent additional relaxation in terms of atomic positions before adatom calculations. The diffusion
583 barriers of the adatoms on the (001) and (111) surfaces were computed using the climbing image nudge elastic band
584 (Cl-NEB) method as implemented in the VASP Transition State Tools (VTSV) code.[57]
585

ASSOCIATED CONTENT

Supporting Information.

Supporting information is available free of charge on the ACS publication website:

Supplementary Figure 1: morphology of as-prepared $Pt_{85}Fe_{15}$ NPs.

Supplementary Figure 2: atomic-scale TEM/STEM images showing the presence of atomic defects along the surface facets of as-synthesized $Pt_{85}Fe_{15}$ NPs.

Supplementary Figure 3: energy-dispersive X-ray spectrum (EDS) of Pt_3Fe NPs.

Supplementary Figure 4: HAADF images of NPs at various annealing temperatures.

Supplementary Figure 5: HAADF-STEM and SE images of formed necks.

Supplementary Figure 6: real-time observations of atomic evaporation-induced particle sintering.

Supplementary Figure 7: HAADF images of formed "bridge-like" necks.

Supplementary Figure 8: DFT calculations of energy barriers for surface detachment and surface diffusion.

Supplementary Figures 9, 10: MD simulations depicting the temperature and inter-particle distance dependence of neck formation.

Supplementary Movie 1 (from which Fig. 3 is extracted): *In situ* HRTEM visualization of NP sintering at T ≈ 500 °C.

Supplementary Movie 2 (from which Fig. 4a-e is extracted): *In situ* HRTEM imaging of the formation of a low-angle grain boundary in the necked region during NP sintering at T ≈ 500 °C.

Supplementary Movie 3 (from which Fig. 4g-k is extracted): *In situ* HRTEM imaging of the formation of a high-angle grain boundary in the necked region during NP sintering at T ≈ 500 °C.

AUTHOR INFORMATION

Corresponding Author

* gzhou@binghamton.edu.

Notes

The authors declare no competing interests.

Acknowledgement

This work was supported by the National Science Foundation (NSF) under the NSF Collaborative Research Award grant DMR 1905422 and 1905572. C.L. and J.F. acknowledge support by the NSF (DMR 1808383 and DMR-2347030) and S3IP/ADL at Binghamton University. Y.Y. and Y.J.H. acknowledge the startup fund support from Drexel University. The computational simulations were carried out using the Drexel's University Research Computing Facility and the Extreme Science and Engineering Discovery Environment (XSEDE) Stampede2 at the TACC through allocation MAT220033 from the Advanced Cyberinfrastructure Coordination Ecosystem: Services & Support (ACCESS) program, which is supported by National Science Foundation Grants #2138259, #2138286, #2138307, #2137603, and #2138296. This research used Electron Microscopy Facilities of the Center for Functional Nanomaterials, which is a US DOE Office of Science User Facility at Brookhaven National Laboratory under contract DE-SC0012704.

References

(1) Zhou, M.; Li, C.; Fang, J. Noble-Metal Based Random Alloy and Intermetallic Nanocrystals: Syntheses and Applications. *Chem. Rev.* **2021**, *121* (2), 736–795.

(2) Cao, S.; Tao, F. F.; Tang, Y.; Li, Y.; Yu, J. Size- and Shape-Dependent Catalytic Performances of Oxidation and Reduction Reactions on Nanocatalysts. *Chem. Soc. Rev.* **2016**, *45* (17), 4747–4765.

(3) Porter, N. S.; Wu, H.; Quan, Z.; Fang, J. Shape-Control and Electrocatalytic Activity-Enhancement of Pt-Based Bimetallic Nanocrystals. *Acc. Chem. Res.* **2013**, *46* (8), 1867–1877.

(4) Datye, A. K.; Xu, Q.; Kharas, K. C.; McCarty, J. M. Particle Size Distributions in Heterogeneous Catalysts: What Do They Tell Us about the Sintering Mechanism? *Catal. Today* **2006**, *111* (1–2), 59–67.

(5) Campbell, C. T.; Parker, S. C.; Starr, D. E. The Effect of Size-Dependent Nanoparticle Energetics on Catalyst Sintering. *Science.* **2002**, *298* (5594), 811–814.

(6) Campbell, C. T. The Energetics of Supported Metal Nanoparticles: Relationships to Sintering Rates and Catalytic Activity. *Acc. Chem. Res.* **2013**, *46* (8), 1712–1719.

(7) Hansen, T. W.; Delariva, A. T.; Challa, S. R.; Datye, A. K. Sintering of Catalytic Nanoparticles: Particle Migration or Ostwald Ripening? *Acc. Chem. Res.* **2013**, *46* (8), 1720–1730.

(8) Li, J.; Deepak, F. L. In Situ Kinetic Observations on Crystal Nucleation and Growth. *Chem. Rev.* **2022**, *122* (23), 16911–16982.

(9) Hwang, S.; Chen, X.; Zhou, G.; Su, D. In Situ Transmission Electron Microscopy on Energy-Related Catalysis. *Adv. Energy Mater.* **2020**, *10* (11), 1902105.

(10) Van Huis, M. A.; Kunneman, L. T.; Overgaag, K.; Xu, Q.; Pandraud, G.; Zandbergen, H. W.; Vanmaekelbergh, D. Low-Temperature Nanocrystal Unification through Rotations and Relaxations Probed by in Situ Transmission Electron Microscopy. *Nano Lett.* **2008**, *8* (11), 3959–3963.

(11) Tian, Y.; Jiao, W.; Liu, P.; Song, S.; Lu, Z.; Hirata, A.; Chen, M. Fast Coalescence of Metallic Glass Nanoparticles. *Nat. Commun.* **2019**, *10*, 5249.

(12) Li, J.; Chen, J.; Wang, H.; Chen, N.; Wang, Z.; Guo, L.; Deepak, F. L. In Situ Atomic-Scale Study

of Particle-Mediated Nucleation and Growth in Amorphous Bismuth to Nanocrystal Phase Transformation. *Adv. Sci.* **2018**, *5* (6), 1700992.

(13) Yao, Y.; Huang, Z.; Xie, P.; Lacey, S. D.; Jacob, R. J.; Xie, H.; Chen, F.; Nie, A.; Pu, T.; Rehwoldt, M.; Yu, D.; Zachariah, M. R.; Wang, C.; Shahbazian-Yassar, R.; Li, J.; Hu, L. Carbothermal Shock Synthesis of High-Entropy-Alloy Nanoparticles. *Science.* **2018**, *359* (6383), 1489–1494.

(14) DeLaRiva, A. T.; Hansen, T. W.; Challa, S. R.; Datye, A. K. In Situ Transmission Electron Microscopy of Catalyst Sintering. *J. Catal.* **2013**, *308*, 291–305.

(15) Zhao, H.; Zhu, Y.; Ye, H.; He, Y.; Li, H.; Sun, Y.; Yang, F.; Wang, R. Atomic-Scale Structure Dynamics of Nanocrystals Revealed By In Situ and Environmental Transmission Electron Microscopy. *Adv. Mater.* **2023**, *35* (50), 2206911.

(16) Boyes, E. D.; LaGrow, A. P.; Ward, M. R.; Martin, T. E.; Gai, P. L. Visualizing Single Atom Dynamics in Heterogeneous Catalysis Using Analytical In Situ Environmental Scanning Transmission Electron Microscopy. *Philos. Trans. R. Soc. A* **2020**, *378* (2186), 20190605.

(17) Simonsen, S. B.; Chorkendorff, I.; Dahl, S.; Skoglundh, M.; Sehested, J.; Helveg, S. Direct Observations of Oxygen-Induced Platinum Nanoparticle Ripening Studied by In Situ TEM. *J. Am. Chem. Soc.* **2010**, *132* (23), 7968–7975.

(18) Yue, S.; Yuan, W.; Deng, Z.; Xi, W.; Shen, Y. In Situ TEM Observation of the Atomic Transport Process during the Coalescence of Au Nanoparticles. *Nano Lett.* **2022**, *22* (20), 8115–8121.

(19) Song, M.; Zhou, G.; Lu, N.; Lee, J.; Nakouzi, E.; Wang, H.; Li, D. Oriented Attachment Induces Fivefold Twins by Forming and Decomposing High-Energy Grain Boundaries. *Science.* **2020**, *367* (6473), 40–45.

(20) Hussein, H. E. M.; Maurer, R. J.; Amari, H.; Peters, J. J. P.; Meng, L.; Beanland, R.; Newton, M. E.; Macpherson, J. V. Tracking Metal Electrodeposition Dynamics from Nucleation and Growth of a Single Atom to a Crystalline Nanoparticle. *ACS Nano* **2018**, *12* (7), 7388–7396.

(21) Yuan, W.; Zhang, D.; Ou, Y.; Fang, K.; Zhu, B.; Yang, H.; Hansen, T. W.; Wagner, J. B.; Zhang, Z.; Gao, Y.; Wang, Y. Direct In Situ TEM Visualization and Insight into the Facet-Dependent

Sintering Behaviors of Gold on TiO_2. *Angew. Chemie* **2018**, *130* (51), 17069–17073.

(22) Li, G.; Fang, K.; Chen, Y.; Ou, Y.; Mao, S.; Yuan, W.; Wang, Y.; Yang, H.; Zhang, Z. Unveiling the Gas-Dependent Sintering Behavior of Au-TiO_2 Catalysts via Environmental Transmission Electron Microscopy. *J. Catal.* **2020**, *388*, 84–90.

(23) Cabello Galisteo, F.; Mariscal, R.; López Granados, M.; Fierro, J. L. G.; Daley, R. A.; Anderson, J. A. Reactivation of Sintered Pt/Al_2O_3 Oxidation Catalysts. *Appl. Catal. B Environ.* **2005**, *59* (3–4), 227–233.

(24) Tomita, A.; Miki, T.; Tai, Y. Effect of Water Treatment and Fe Doping on Pt Sintering and the Propane Oxidation Activity of Pt/Al_2O_3. *Appl. Catal. A Gen.* **2016**, *522*, 138–144.

(25) Yin, P.; Hu, S.; Qian, K.; Wei, Z.; Zhang, L. Le; Lin, Y.; Huang, W.; Xiong, H.; Li, W. X.; Liang, H. W. Quantification of Critical Particle Distance for Mitigating Catalyst Sintering. *Nat. Commun.* **2021**, *12*, 4865.

(26) Qing, S.; Hou, X.; Li, L.; Feng, G.; Wang, X.; Gao, Z.; Fan, W. Deactivation Feature of Cu/SiO_2 Catalyst in Methanol Decomposition. *Int. J. Hydrogen Energy* **2019**, *44* (31), 16667–16674.

(27) Sehested, J.; Gelten, J. A. P.; Remediakis, I. N.; Bengaard, H.; Nørskov, J. K. Sintering of Nickel Steam-Reforming Catalysts: Effects of Temperature and Steam and Hydrogen Pressures. *J. Catal.* **2004**, *223* (2), 432–443.

(28) Jin, B.; Sushko, M. L.; Liu, Z.; Jin, C.; Tang, R. In Situ Liquid Cell TEM Reveals Bridge-Induced Contact and Fusion of Au Nanocrystals in Aqueous Solution. *Nano Lett.* **2018**, *18* (10), 6551–6556.

(29) Schlexer, P.; Andersen, A. B.; Sebok, B.; Chorkendorff, I.; Schiøtz, J.; Hansen, T. W. Size-dependence of the Melting Temperature of Individual Au Nanoparticles. *Part. Part. Syst. Charact.* **2019**, *36* (3), 1800480.

(30) Simonsen, S. B.; Chorkendorff, I.; Dahl, S.; Skoglundh, M.; Helveg, S. Coarsening of Pd Nanoparticles in an Oxidizing Atmosphere Studied by in Situ TEM. *Surf. Sci.* **2016**, *648*, 278–283.

(31) Simonsen, S. B.; Chorkendorff, I.; Dahl, S.; Skoglundh, M.; Sehested, J.; Helveg, S. Ostwald Ripening in a Pt/SiO_2 Model Catalyst Studied by in Situ TEM. *J. Catal.* **2011**, *281* (1), 147–155.

(32) Asoro, M. A.; Ferreira, P. J.; Kovar, D. In Situ Transmission Electron Microscopy and Scanning Transmission Electron Microscopy Studies of Sintering of Ag and Pt Nanoparticles. *Acta Mater.* **2014**, *81*, 173–183.

(33) Zhou, W. L.; He, J.; Fang, J.; Huynh, T. A.; Kennedy, T. J.; Stokes, K. L.; O'Connor, C. J. Self-Assembly of FePt Nanoparticles into Nanorings. *J. Appl. Phys.* **2003**, *93* (10 2), 7340–7342.

(34) Kim, J.; Lee, Y.; Sun, S. Structurally Ordered FePt Nanoparticles and Their Enhanced Catalysis for Oxygen Reduction Reaction. *J. Am. Chem. Soc.* **2010**, *132* (14), 4996–4997.

(35) Li, Q.; Wu, L.; Wu, G.; Su, D.; Lv, H.; Zhang, S.; Zhu, W.; Casimir, A.; Zhu, H.; Mendoza-Garcia, A.; Sun, S. New Approach to Fully Ordered Fct-FePt Nanoparticles for Much Enhanced Electrocatalysis in Acid. *Nano Lett.* **2015**, *15* (4), 2468–2473.

(36) Reiss, G.; Hütten, A. Applications beyond Data Storage. *Nat. Mater.* **2005**, *4* (10), 725–726.

(37) Chen, X.; Zhang, S.; Li, C.; Liu, Z.; Sun, X.; Cheng, S.; Zakharov, D. N.; Hwang, S.; Zhu, Y.; Fang, J.; Wang, G.; Zhou, G. Composition-Dependent Ordering Transformations in Pt-Fe Nanoalloys. *Proc. Natl. Acad. Sci. U. S. A.* **2022**, *119* (14), e2117899119.

(38) Ashcroft, N. W.; Denton, A. R. Vegard's Law. *Phys. Rev. A* **1991**, *43* (6), 3161–3164.

(39) Hovorka, O.; Devos, S.; Coopman, Q.; Fan, W. J.; Aas, C. J.; Evans, R. F. L.; Chen, X.; Ju, G.; Chantrell, R. W. The Curie Temperature Distribution of FePt Granular Magnetic Recording Media. *Appl. Phys. Lett.* **2012**, *101* (5), 052406.

(40) Rong, C. B.; Li, Y.; Liu, J. P. Curie Temperatures of Annealed FePt Nanoparticle Systems. *J. Appl. Phys.* **2007**, *101* (9), 09K505.

(41) Frey, H.; Beck, A.; Huang, X.; van Bokhoven, J. A.; Willinger, M. G. Dynamic Interplay between Metal Nanoparticles and Oxide Support under Redox Conditions. *Science.* **2022**, *376* (6596), 982–987.

(42) Lunkenbein, T.; Schumann, J.; Behrens, M.; Schlögl, R.; Willinger, M. G. Formation of a ZnO Overlayer in Industrial Cu/ZnO/Al_2O_3 Catalysts Induced by Strong Metal-Support Interactions . *Angew. Chemie* **2015**, *127* (15), 4627–4631.

(43) Penn, R. L.; Banfield, J. F. Imperfect Oriented Attachment: Dislocation Generation in Defect-Free Nanocrystals. *Science.* **1998**, *281* (5379), 969–971.

(44) Bronstein, L. M.; Huang, X.; Retrum, J.; Schmucker, A.; Pink, M.; Stein, B. D.; Dragnea, B.; December, R. V; Re, V.; Recei, M.; April, V.; Wang, F.; Richards, V. N.; Shields, S. P.; Buhro, W. E.; Jin, Y.; Yi, Q.; Ren, Y.; Wang, X.; Ye, Z.; Chang, J.; Waclawik, E. R.; Zhong, X.; Feng, Y.; Zhang, Y.; Lieberwirth, I.; Knoll, W.; Ito, D.; Yokoyama, S.; Zaikova, T.; Masuko, K.; Hutchison, J. E.; Li, D.; Nielsen, M. H. M. H.; Lee, J. R. I. J. R. I.; Frandsen, C.; Banfield, J. F.; De Yoreo, J. J. Direction-Specific Interactions. *Science.* **2012**, *336* (6084), 1014–1018.

(45) De Yoreo, J. J.; Gilbert, P. U. P. A.; Sommerdijk, N. A. J. M.; Penn, R. L.; Whitelam, S.; Joester, D.; Zhang, H.; Rimer, J. D.; Navrotsky, A.; Banfield, J. F.; Wallace, A. F.; Michel, F. M.; Meldrum, F. C.; Cölfen, H.; Dove, P. M. Crystallization by Particle Attachment in Synthetic, Biogenic, and Geologic Environments. *Science.* **2015**, *349* (6247), aaa6760.

(46) Asoro, M. A.; Kovar, D.; Shao-Horn, Y.; Allard, L. F.; Ferreira, P. J. Coalescence and Sintering of Pt Nanoparticles: In Situ Observation by Aberration-Corrected HAADF STEM. *Nanotechnology* **2010**, *21* (2), 025701.

(47) Asoro, M. A.; Ferreira, P. J.; Kovar, D. In Situ Transmission Electron Microscopy and Scanning Transmission Electron Microscopy Studies of Sintering of Ag and Pt Nanoparticles. *Acta Mater.* **2014**, *81*, 173–183.

(48) Zhang, J.; Fang, J. A General Strategy for Preparation of Pt 3d-Transition Metal (Co, Fe, Ni) Nanocubes. *J. Am. Chem. Soc.* **2009**, *131* (51), 18543–18547.

(49) Kryuchkov, N. P.; Yurchenko, S. O.; Fomin, Y. D.; Tsiok, E. N.; Ryzhov, V. N. Complex Crystalline Structures in a Two-Dimensional Core-Softened System. *Soft Matter*. **2018**, 14, 2152–2162.

(50) Kim, J.; Koo, Y.; Lee, B.-J. Modified Embedded-Atom Method Interatomic Potential for the Fe–Pt Alloy System. *J. Mater. Res.* **2006**, *21* (1), 199–208.

(51) Rahm, J. M.; Erhart, P. WulffPack: A Python Package for Wulff Constructions. *J. Open Source*

Softw. **2020**, *5* (45), 1944.

(52) Kresse, G.; Furthmü, J. Efficient Iterative Schemes for Ab Initio Total-Energy Calculations Using a Plane-Wave Basis Set. *Phys. Rev. B* **1996**, *54* (16), 11169-11186.

(53) Blöchl, P. E. Projector Augmented-Wave Method. *Phys. Rev. B* **1994**, *50* (24), 17953–17979.

(54) Perdew, J. P.; Burke, K.; Ernzerhof, M. Generalized Gradient Approximation Made Simple. *Phys. Rev. Lett.* **1996**, *77* (18), 3865–3868.

(55) Scott Weingarten, N.; Byrd, E. F. C. Special Quasirandom Structures of Alon. *Comput. Mater. Sci.* **2015**, *96*, 312–318.

(56) Van De Walle, A.; Tiwary, P.; De Jong, M.; Olmsted, D. L.; Asta, M.; Dick, A.; Shin, D.; Wang, Y.; Chen, L. Q.; Liu, Z. K. Efficient Stochastic Generation of Special Quasirandom Structures. *Calphad Comput. Coupling Phase Diagrams Thermochem.* **2013**, *42*, 13–18.

(57) Henkelman, G.; Uberuaga, B. P.; Jónsson, H. Climbing Image Nudged Elastic Band Method for Finding Saddle Points and Minimum Energy Paths. *J. Chem. Phys.* **2000**, *113* (22), 9901–9904.

Table of contents